# Probing neural networks with t-SNE, class-specific projections and a guided tour

Christopher R. Hoyt Stanford University Art B. Owen Stanford University

July 2021

#### Abstract

We use graphical methods to probe neural nets that classify images. Plots of t-SNE outputs at successive layers in a network reveal increasingly organized arrangement of the data points. They can also reveal how a network can diminish or even forget about within-class structure as the data proceeds through layers. We use class-specific analogues of principal components to visualize how succeeding layers separate the classes. These allow us to sort images from a given class from most typical to least typical (in the data) and they also serve as very useful projection coordinates for data visualization. We find them especially useful when defining versions guided tours for animated data visualization.

### 1 Introduction

Probing is a term used to describe certain exploratory analyses of neural networks. It allows the user to see what happens as the number of layers used [1] or amount of training time taken [14] increases. Nguyen et al. [13] consider changes to both depth and breadth of networks. One could also study changes to a network as the volume of training data increases.

Alain and Bengio [1] investigate networks of L layers by passing the output of the first  $\ell < L$  layers through a specially retrained softmax layer as the  $\ell + 1$ 'st and final layer. They can then study the progress that the network makes as layers are added. They have the interesting observation that the information content in layer  $\ell + 1$  can be less than what is in layer  $\ell$  but not more, and yet accuracy may improve because the information has a better representation at later layers.

In this work, we present some tools for graphically probing neural nets. The nets we study as examples are designed to classify an image into one of K classes. Instead of passing the output of an intermediate layer through a special softmax layer we explore each layer's output visually. First, we run t-SNE [17] on the outputs of intermediate layers. Sometimes we see interesting phenomena in the intermediate layers that have disappeared by the final layers. For instance, within-class clustering could be evident in the early layers but forgotten by the final layer without harming the final classification accuracy that the network was trained to optimize.

Next, we look at principal components (PC) projections of intermediate layer results. By watching how those change from layer to layer we can see how the group separations evolve. The PC projections have the advantage that we can project additional points, such as held out data points, onto their coordinates. This is different from t-SNE where including additional points would change the mapping of all the points. Also, PC mappings are deterministic given the data, and hence more reproducible, while the t-SNE images are randomly generated. We do not always see the neural collapse phenomenon from [14]. That analysis predicts that the neuron outputs for different categories will end up as roughly spherical clusters at the corners of a simplex. Instead of clusters we often see ellipsoids extending from such a corner towards the origin. Neural collapse predicts an angle of about 90 degrees between clusters. We see that this emerges as layers progress, but in early layers than angle can be much less. In intermediate layers we often see angles much greater than 90 degrees as if hard to separate classes are being treated as opposites.

When there are many classes, principal components trained on all of them can make it harder to spot patterns among a few commonly confused classes. We could get better resolution by defining principal components tuned to one subset of classes. That, however, requires a separate PCA analysis for every subset of variables. We have found it beneficial to define one class-specific vector per output class in a way that is analogous to the PC eigenvectors. Then each subset of categories comes with a prescribed set of vectors for projection. Similar class-specific vectors were previously studied by Krzanowski [11] but that work was not about visualization. We can also use these vectors to rank input images from most typical to least typical members of their respective classes. Note that typical is defined with respect to the set of images gathered for training and those images might not remain typical when an algorithm is deployed.

We also consider some animated tours [2, 3] of data at each level where we probe. Li et al. [12] previously used grand tours on the output of a neural network. In the terminology of [3] our tours are guided tours: we select pairs of interesting projections and interpolate between them. We develop guided tours based on class-specific projections of data including looks at intermediate layers.

We use two well studied neural networks as running examples. One is the CIFAR-10 dataset [9] of sixty thousand 32 by 32 color images selected from 10 classes consisting of four mechanical groups (e.g., airplanes and automobiles) and six animal groups (e.g., cats and dogs). For this we use the network and trained weights from https://github.com/geifmany/cifar-vgg which utilizes the VGG model with 15 layers. VGG stands for the 'visual geometry group' at Oxford who developed the architecture. The other example is the fashion-MNIST data with sixty thousand 28 by 28 grayscale images selected from 10 classes of clothing items (like trousers and pullovers), which was then subsequently padded out with zeros along the edges to become 32 by 32 images with three channels. For this we consider the ResNet50 network architecture [8] with weights initialized from ImageNet pretraining [6].

The outline of this paper is as follows. Section 2 gives background about the neural networks we explore. Section 3 shows a use of t-SNE for probing. We can see how class separation progresses as the layers increase. Section 4 defines our class-specific vectors and compares plots in those coordinates to principal components plots. Section 5 describes our class-specific tours. It include still shots of the tours and a link to animated versions. Section 6 describes how our class-specific vectors can potentially identify separations of groups within a single classification.

#### 2 Image data sets, architectures, and

The network we use for CIFAR-10 from https://github.com/geifmany/cifar-vgg has thirteen convolution layers and two fully connected layers that we study. Those are layers

$$\ell = 2, 6, 9, 14, 18, 22, 26, 30, 34, 38, 42, 46, 50, 56, 60$$

of that network. Figure 1 shows their positions in the overall architecture. We probed the network outputs at these layers by passing the output from layer  $\ell$  through a specially trained final softmax layer. Figure 2 plots the accuracy attained this way versus the layer indices. What we see is that the accuracy on test data increased up to layer 30, and subsequent layers did not improve it by much. The accuracy on the training data saturated at 100% by layer 18. In a Shapley value analysis (to be reported elsewhere) we found that of these layers, layer 2 was most important for ultimate accuracy. At layer 2, the network is not anywhere near it's final accuracy.

For fashion-MNIST we used the ResNet50 architecture from [8] which has 177 layers. See Figure 3. We probed the network at the outputs of the sixteen convolution / identity blocks, corresponding to layers

 $\ell = 17, 27, 37, 49, 59, 69, 79, 91, 101, 111, 121, 131, 141, 153, 163, 173.$ 

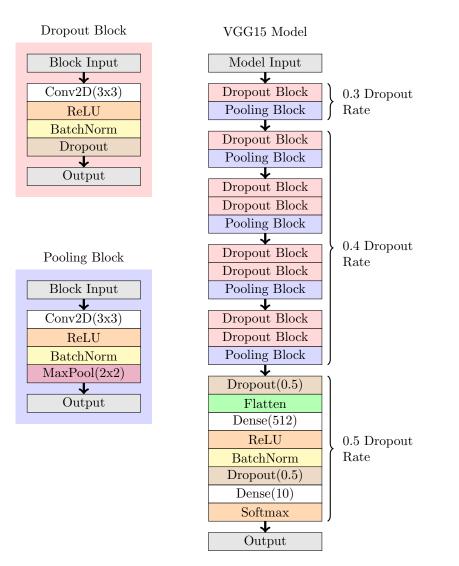


Figure 1: The model architecture for the VGG15 model. The model consists of thirteen convolution layers and two dense layers, creating fifteen natural checkpoints for the model overall. Refer to https://github.com/geifmany/cifar-vgg for more specific details on the model architecture.

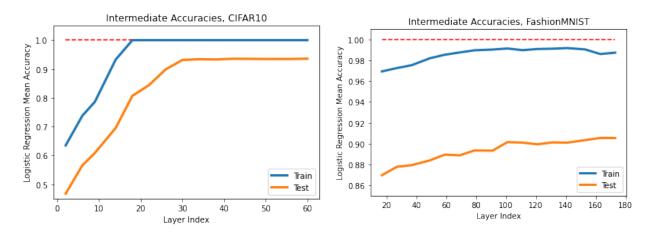


Figure 2: Intermediate accuracies of the models used for the CIFAR10 and FashionMNIST datasets using a logistic regression trained on a random subset of n = 10,000 samples from the training dataset. We plot the accuracy of the model versus layer with one curve for the training inputs and another for the test inputs.

	Predicted class										
True class	plane	car	bird	$\operatorname{cat}$	deer	$\log$	frog	horse	ship	truck	
plane	924	2	20	4	3	0	1	3	36	7	
car	3	972	0	0	0	1	0	0	5	19	
bird	13	0	929	11	16	10	11	5	5	0	
$\operatorname{cat}$	5	0	24	848	12	88	14	3	4	2	
deer	3	0	12	16	946	10	5	8	0	0	
$\log$	2	2	11	68	11	895	2	6	1	2	
frog	4	1	14	12	2	5	961	0	1	0	
horse	5	1	9	6	8	12	0	958	0	1	
$_{\rm ship}$	7	0	2	4	1	1	1	0	979	5	
truck	9	26	0	2	1	2	0	1	12	947	

Table 1: This is the confusion matrix for the CIFAR10 test data.

The accuracy attained by adjoining a softmax layer after layer  $\ell$  is plotted versus  $\ell$  in Figure 2. There we do not see the rapid initial gain in accuracy versus  $\ell$ . We attribute this difference to that network having been initialized with values from training on ImageNet [6].

The confusion matrix for the CIFAR10 data is in Table 1. Separating cat images from dog images appears to be the hardest task. Trucks and cars are also frequently confused with each other. Many planes are labeled as ships but the reverse is less common. Table 2 shows the confusion matrix for the FashionMNIST data. Coats and pullovers are commonly confused with each other as are ankle boots and sneakers, while shirts are confused with four other classes.

### 3 Probing with t-SNE

An alternative to training an  $\ell+1$ 'st layer is to use t-SNE on the  $N \times M_{\ell}$  matrix of output at layer  $\ell$ . The t-SNE algorithm produces a lower dimensional representation of the points, that like multidimensional scaling [16, 10, 5] seeks to have low dimensional interpoint distances be representative of the original

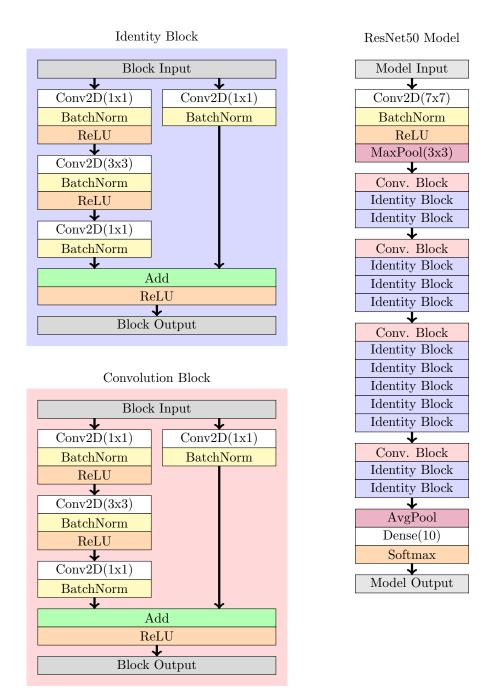


Figure 3: ]The model architecture for the ResNet50 model. The model starts off with an initial processing section, and then proceeds with a series of 16 residual units (the identity and convolution blocks). As we progress through the blocks, we decrease the width and height of the inputs and increase the number of channels. Refer to [8] for more specific details on the model architecture.

	Predicted class											
True class	t-shirt/top	trouser	pullover	dress	coat	sandal	$\operatorname{shirt}$	sneaker	bag	ankle		
t-shirt/top	873	1	12	12	4	1	94	0	3	0		
trouser	1	987	1	6	1	0	2	0	2	0		
pullover	15	1	879	10	43	0	51	0	1	0		
dress	14	6	7	919	26	0	26	1	0	1		
coat	0	0	55	24	878	0	43	0	0	0		
sandal	0	0	0	0	0	983	0	15	0	2		
shirt	86	3	47	19	69	0	768	0	8	0		
sneaker	0	0	0	0	0	8	0	973	0	19		
bag	3	2	1	1	3	1	2	3	983	1		
ankle boot	0	0	0	0	0	5	1	32	0	962		

Table 2: This is the confusion matrix for the FashionMNIST test data.

higher dimensional interpoint distances. It also emphasizes smaller interpoint distances as in local multidimensional scaling [4]. The algorithm proceeds without knowing the classifications of the data or even the number K of levels of the categorical response. Following [7] we projected the  $M_{\ell}$  dimensional points onto their first 50 principal components before running t-SNE. The t-SNE algorithm involves some randomness. Its criterion is also invariant to rotations or reflections of the point clouds. In order to make the images more nearly comparable we used the same random seed at each layer. Furthermore, the practice of projecting the intermediate outputs down to the same dimension, 50, using PCA in each case makes the starting points for the layers more closely aligned with each other than they would otherwise be. The lone exception to the above description is for the output of layer 60 of the VGG15 model for the CIFAR10 dataset. This output is 10-dimensional as it is the output of the entire network with one value per class. In this case, we use all 10 dimensions in the t-SNE algorithm. Because t-SNE's criterion is dominated by small interpoint distances, the precise location and orientation of a cluster well separated from the rest of the data could be strongly influenced by the random seed. The relative position of clusters that overlap or nearly do is likely to be a more stable feature.

Figures 4, 5, and 6 show t-SNE outputs for the fashion-MNIST data. These images depict the held out, testing data, not the training data. Up to and including layer 49, the images for 'bag' clearly plot as two disjoint and even widely separated clusters. Inspection in Section 6 reveals that there are two kinds of bag image, one that we could call purses and another that mixes clutchs and satchels. By purse images we mean those with handles/straps that are well separated from and above the rest of the bag. The clutchs don't have straps, while the satchels have straps that are nearly adjacent to the rest of the bag. Interestingly, by about layer 91 the two 'bag' groups have connected and by around layer 163 or 173 they appear to have merged into one. The loss function used in training does not reward the network for noticing that there are two kinds of bag and, as it happens, that distinction weakens or even disappears from the t-SNE plot.

In Section 6 we use a method of ranking images from most like their own class to least like their own class. We find that there are also two very different kinds of sandal images and possibly two very different kinds of trouser images. Figures 14, 15 and 16 there depict examples of extreme bags, sandals and trousers.

We also see in Figures 4, 5, and 6 that the trouser and to a lesser extent bag images are already well separated from the other classes by layer 17. The footwear groups (sandals, sneakers, and ankle boots) start very connected with one another until sandals separate by layer 69, and the sneakers and ankle boots separate from one another by layer 101. Similarly, the upper body wear classes (t-shirt/tops, pullovers, dresses, coats, shirts) start out well merged, and only really separate out from one another towards the very end at layer 173.

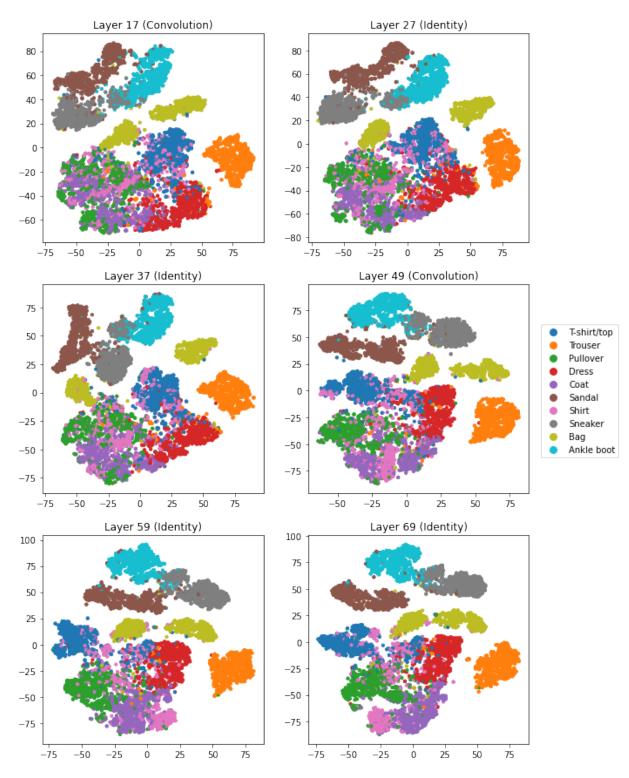


Figure 4: t-SNE output for FashionMNIST data after layers 17, 27, 37, 49, 59, and 69. The types of these blocks are listed above in the titles.

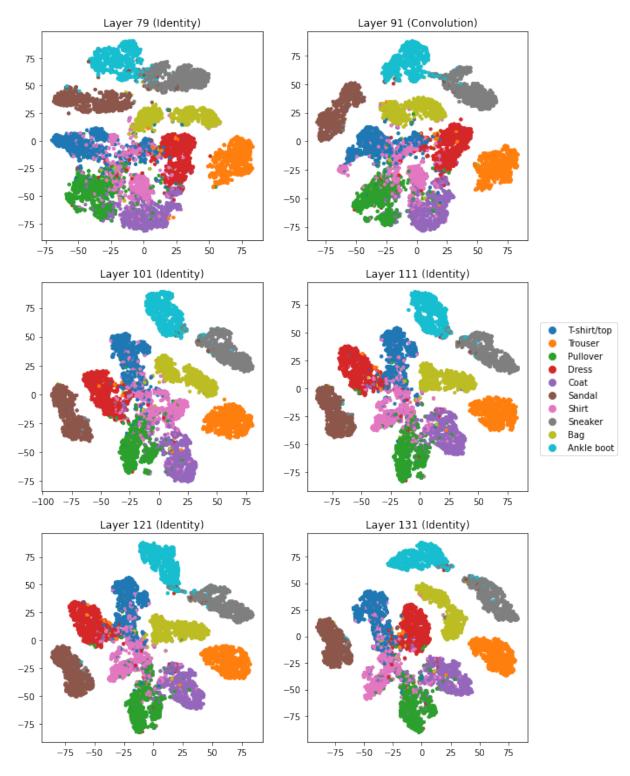


Figure 5: t-SNE output for FashionMNIST data after layers 79, 91, 101, 111, 121, and 131. The types of these blocks are listed above in the titles.

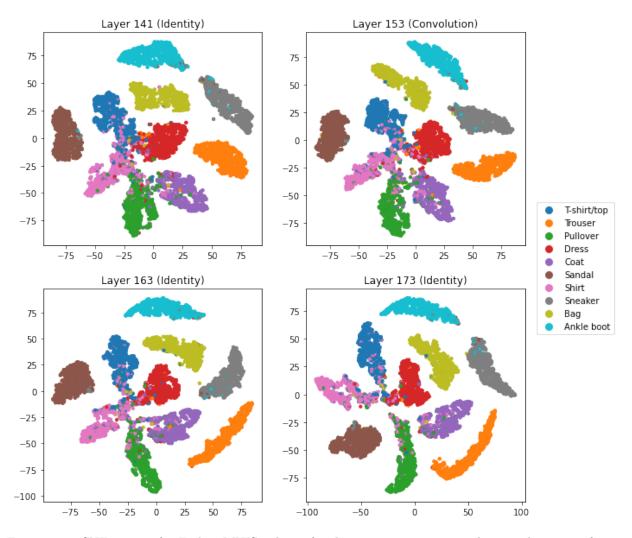


Figure 6: t-SNE output for FashionMNIST data after layers 141, 153, 163, and 173. The types of these blocks are listed above in the titles.

Figures 7 and 8 show the corresponding t-SNE plots for the CIFAR-10 data at 12 different output layers ranging from layer 14 to layer 60. A striking difference in these figures is that in the early layers (14 and 18) the points are not at all separated into disjoint clouds. Recall that the fashion-MNIST network was initialized to weights from training in ImageNet. The network for CIFAR-10 by contrast was trained from a random start. By layer 30 we start to see groups forming though there is still a lot of overlap. Cats and dogs remain closely connected up to and including layer 56, the second last one shown. Recall that from the confusion matrices, separating cats from dogs is especially hard.

By the final layer 60, the 10 classes are very well separated in a two dimensional view, forming narrow and bent clusters. There are still errors in the classification. Many of those points plot within clusters for another category, very often near one of the tips and very often nearer the center of the image. That latter pattern was more pronounced for FashionMNIST. In the t-SNE for layer 60, cat and dog clusters are well separated but some of the cat images are at one end of the dog image cluster. On inspection we find that these points were misclassified but with high confidence.

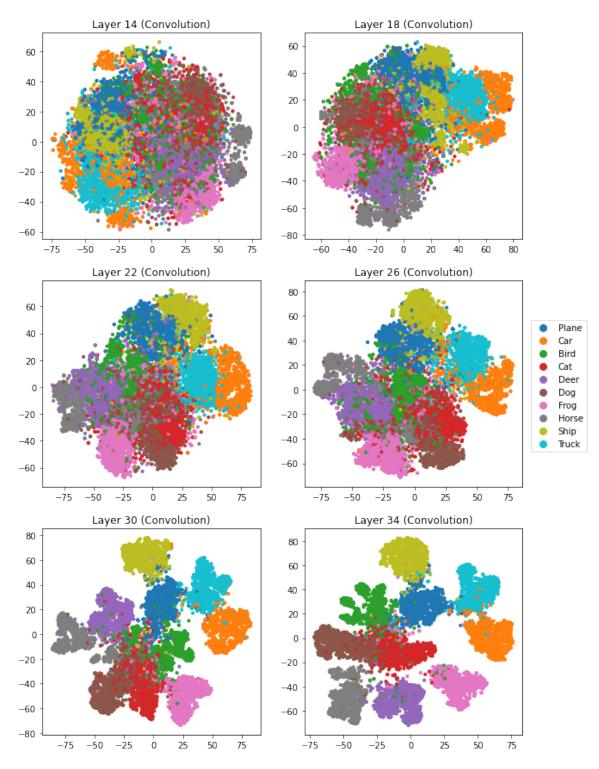


Figure 7: t-SNE output for CIFAR10 data after layers 14, 18, 22, 26, 30, and 34. The types of these layers are listed above in the titles.

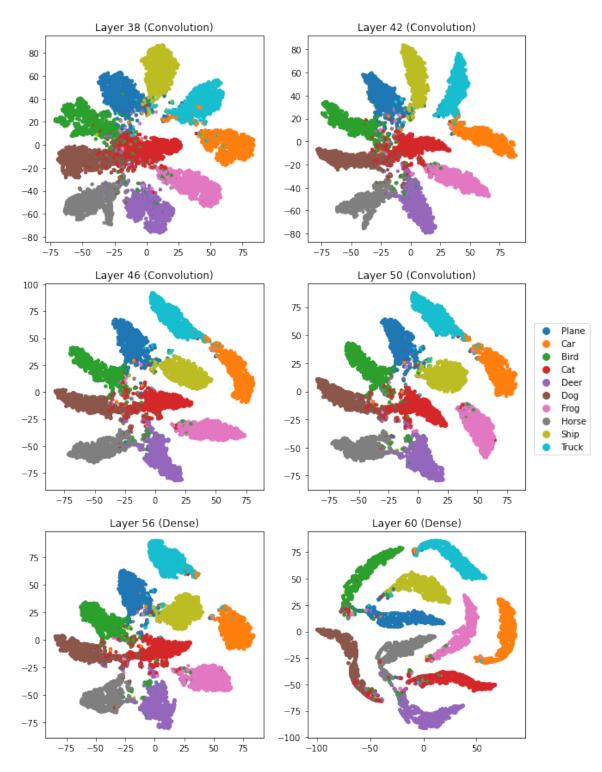


Figure 8: t-SNE output for CIFAR10 data after layers 38, 42, 46, 50, 56, and 60. The types of these layers are listed above in the titles.

### 4 Class specific vectors

While t-SNE is powerful and evocative, the spatial placement of individual points is hard to interpret. A principal components analysis offers some alternative functionality. Given the data, the PC mapping is not random, so the position of points is more reproducible and in particular, the closeness of clusters is not subject to algorithmic noise. Second, having constructed principal components for one set of data, we can project additional data onto them. For instance we could define principal components using the training data and, retaining those eigenvectors, project test data into the same space.

The data we use are  $X \in \mathbb{R}^{N \times M}$  and  $Y \in \{0, 1, \dots, K-1\}^N$ . The matrix X changes from layer to layer as does M, while Y remains constant. Each column of X represents the output from one neuron in the layer under study. We center these outputs by subtracting the mean from each column of X. That way we ensure that  $\sum_{i=1}^{N} x_i = \mathbf{0} \in \mathbb{R}^M$  where  $x_i \in \mathbb{R}^M$  is the *i*'th row of X expressed as a column vector.

We are interested to see the arrangements among commonly confused classes. For instance, it is of interest to see the relative arrangements among the mechanical images because there are frequent errors within those classes. Figure 9 shows the global principal components plots for the outputs of only the groups of ships, planes, cars, and trucks in CIFAR10. What we see there is that projecting all ten classes at once yields a lot of overlap. We get a better view from PC plots based on just those classes as in Figure 10. There we see that in the later layers the four classes plot as lengthy ellipsoids from a common origin.

We see that the last pre-softmax layers are mostly consistent with neural collapse [14] in that the vectors for most pairs of groups are nearly orthogonal to each other by the later layers. The clouds do extend towards the origin where we see some overlap.

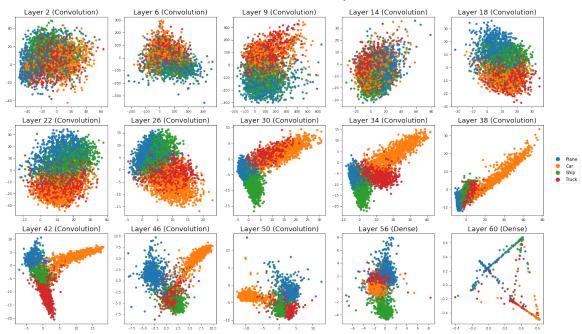
We also see that in layers 30 to 42, the data for images of planes projects to nearly the origin in the first two principal components. Only later do the planes clearly stand out from the other mechanical classes. Layer 60 reflects data after the softmax transformation and it shows clearly that most points have at most one or two non-negligible possibilities because the points are mostly projected from a tetrahedral wireframe pattern.

It is a nuisance to redefine the principal components for every subset of variables that we might wish to explore. We prefer to define class-specific projections of the data. For each  $k \in \{0, 1, \ldots, K-1\}$ we choose a one-dimensional projection especially representative of class k, as described below, and then view the data in projections given by two of those vectors. Class-specific vectors were studied by [11]. That work did not look at them for visualization.

Let  $N_k$  be the number of indices i with  $Y_i = k$ . The matrix  $X_k \in \mathbb{R}^{N_k \times M}$  has all the  $\boldsymbol{x}_i$  for which  $Y_i = 1$ . Now we choose a special vector  $\theta_k \in \mathbb{R}^M$  for cluster k. There are several choices. We could take  $\theta_k$  to be the unit vector proportional to  $(1/N_k) \sum_{i:Y_i=k} \boldsymbol{x}_i$  the mean vector for cluster k. A second choice is the unit vector  $\theta_k = \arg \max_{\|\theta\|=1} \theta^{\mathsf{T}} X_k^{\mathsf{T}} X_k \theta$ . The third choice is the first principal component vector of  $X_k$ . This differs from the second choice in that we must recenter  $X_k$  to make its rows have mean zero, yielding  $\tilde{X}_k$ . Then  $\theta_k$  maximizes  $\theta^{\mathsf{T}} \tilde{X}_k^{\mathsf{T}} \tilde{X}_k \theta$  over unit vectors  $\theta \in \mathbb{R}^M$ . Below we work with the third choice. The vectors we get characterize the principal direction of points within each point cloud, not differences in the per class means.

When we take the within-class principal component vector we have also to choose its sign. If  $\theta$  is the first principal component vector then  $-\theta$  has an equal claim to that label. We choose the sign so that the mean of the data for class k has a larger inner-product with  $\theta$  than the global mean has.

Using class-specific projections, we make scatterplots of  $X\theta_k \in \mathbb{R}^N$  versus  $X\theta_{k'}$  for pairs of classes  $k \neq k'$ . These plots show one point per sample. Figure 11 shows the mechanical images plotted in the space defined by the car versus plane vectors. This is a projection but not an orthogonal projection into  $\mathbb{R}^2$  because  $\theta_k$  and  $\theta_{k'}$  need not be orthogonal. In the early layers, the class-specific projections produce highly correlated scatter plots. This is largely because the vectors  $\theta_k$  and  $\theta_{k'}$  start out correlated. In later layers, points vary greatly in the projections from their own class and much less in the other projections. The class-specific asxes for cars and trucks start off approximately



First Two Global PCA Axes Projection

Figure 9: Projections from the top two principal components in a global PCA for all activation layers, visualizing the planes, cars, ships, and trucks in CIFAR10.

#### First Two Mechanical PCA Axes Projection

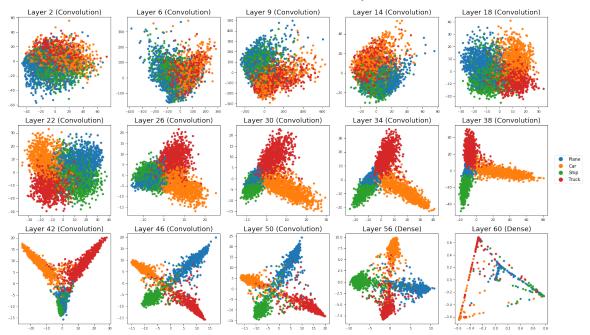


Figure 10: Projections from the top two principal components in a PCA involving only the mechanical groups (planes, cars, ships, and trucks) for the outputs of all activation layers, visualizing the planes, cars, ships, and trucks in CIFAR10.

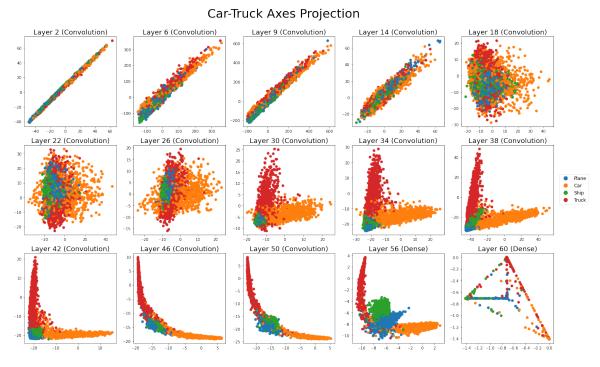


Figure 11: In each plot, the vertical axis has data projected on the class-specific vector for 'car' images and the horizontal axis uses the class-specific vector for 'truck' images. The points are for the plane, car, ship, and truck images in CIFAR10.

parallel start to become nearly orthogonal by layer 18 (though the point clouds still overlap a lot). By layer 30 we see meaningful separations among the points. In layers 46 and 50 it appears that the angle between those clouds is more than 90 degrees. This is confirmed by a tour image (in Section 5) that makes an orthogonal projection of the data into the plane spanned by those two vectors. We also observe that in layers 46, 50, and 56, while the car and truck axes are nearly perpendicular, the clusters of points for these two groups "bend" into one another where they meet.

Car and truck images are fairly similar. At layer 30, we see that trucks tend to plot at positive values along the car axis. By layer 46, trucks are now plotting at negative values along the car axis. The intervening layers have been configured to push those classes farther apart. Planes and ships do not proceed through such a process. Instead they have near zero projections along both car and truck directions through training.

### 5 Class specific guided tour

A tour of  $X \in \mathbb{R}^{N \times M}$  is an animated sequence of projections (also commonly referred to as frames) of X into  $\mathbb{R}^{N \times d}$ , where d is typically a small value such as 2 or 3. The best known of these is the grand tour [2] which generates a sequence of such projections designed to explore the space of all projections by eventually getting close to every point in the manifold of projections from  $\mathbb{R}^M$  to  $\mathbb{R}^d$ . That manifold is quite large, so it can take a long time to get close to every view. Therefore specific tours have been developed to make a more focussed exploration of views. Simple tours generally consist of moving along a sequence of projections using interpolated paths between sequential pairs of projections of interest. The resulting animation rotates smoothly between these pairs. The technical procedure is outlined in Section 4.1 of Buja et al. [3]. Planned tours refer to tours where the (usually finite) sequence of frames are predetermined. To visualize the data, we choose to explore the space created by the span of the ten class-specific vectors. For ease of computation, we fit a PCA with a single component to the class specific data  $X_k \in \mathbb{R}^{N_k \times M}$  to acquire the principle axes  $\theta_k \in \mathbb{R}^M$  and the decomposition of the data onto the class-specific axis  $(X - \mathbf{1}\bar{x}_k^{\mathsf{T}})\theta_k$ , where  $\mathbf{1} \in \mathbb{R}^N$  is the all ones vector. At this point, we flip the value of  $\theta_k$  via products with negative one so that the class mean has a larger dot product with  $\theta_k$  than the global mean, or equivalently that  $(\bar{x} - \bar{x}_k)^{\mathsf{T}}\theta_k < 0$  where  $\bar{x} \in \mathbb{R}^M$  is the global mean. Aggregating this information, we then have collected  $X' = [(X - \mathbf{1}\bar{x}_1^{\mathsf{T}})\theta_1, \ldots, (X - \mathbf{1}\bar{x}_K^{\mathsf{T}})\theta_K] \in \mathbb{R}^{N \times K}$  as well as  $\Theta = [\theta_1, \ldots, \theta_K]$ . We then center X' so that the columns have means zero, producing  $\tilde{X}' = (X - \mathbf{1}\bar{x}^{\mathsf{T}})\Theta$ , which is used as the data to produce the class-specific pair plots.

To produce the tours that leverage the class specific vectors  $\theta_k$ , we apply the technique used in [3] and project the data X into the space spanned by the K class-specific vectors since K is usually much smaller than M. Note that we cannot use tours on  $(X - \mathbf{1}\bar{x}^{\mathsf{T}})\Theta$  directly since this is not an orthogonal projection of the original centered data  $X - \mathbf{1}\bar{x}^{\mathsf{T}}$ . To get around this, we perform the QR-decomposition  $\Theta = Q_{\theta}R_{\theta}$  with  $Q_{\theta} \in \mathbb{R}^{M \times K}$  and  $R_{\theta} \in \mathbb{R}^{K \times K}$ . We then visualize the projection of the data  $(X - \mathbf{1}\bar{x}^{\mathsf{T}})Q_{\theta}$ . If K is much smaller than M and that the class-specific vectors are linearly independent, we can compute this efficiently as  $(X - \mathbf{1}\bar{x}^{\mathsf{T}})\Theta \cdot R_{\theta}^{-1}$  since we already have  $(X - \mathbf{1}\bar{x}^{\mathsf{T}})\Theta$  from the computation for the class specific pair plots.

In the case that the K class-specific vectors are not linearly independent, special considerations need to be made. While most layers do not have this issue, the output layers, such as layer 60 in the VGG15 model, ordinarily do. This is because the output is 10-dimensional with the constraint that the ten components need to add up to one, and thus the space spanned by the ten class specific axes is at most 9-dimensional. In this case, we again compute the QR-decomposition  $\Theta = Q_{\theta}R_{\theta}$ , but we now force  $Q_{\theta} \in \mathbb{R}^{M \times r}$  and  $R_{\theta} \in \mathbb{R}^{r \times K}$  where r is the rank of  $\Theta$  and calculate  $(X - \mathbf{1}\bar{x}^{\mathsf{T}})Q_{\theta}$  directly.

In either case, we note that  $R_{\theta} = Q_{\theta}^{\mathsf{T}} \Theta$  implies that the columns of  $R_{\theta} = [r_1, \ldots, r_K]$  are the projections of each of the class-specific vectors to the space spanned by all of the class-specific vectors. Doing so, we can condense all information about tours in the space spanned by the class specific vectors down to the projections  $(X - \mathbf{1}\bar{x}^{\mathsf{T}})Q_{\theta}$  and  $R_{\theta} = Q_{\theta}^{\mathsf{T}}\Theta$  of the data and the class specific vectors respectively.

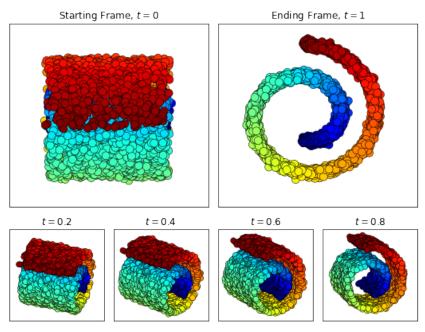
For an animated view of the see

#### https://purl.stanford.edu/zp755hs7798.

Figure 12 shows still images of frames that can be seen on an example toy Swiss Roll dataset. Figure 13 shows frames that can be seen when exploring the VGG15 and ResNet50 models for both training and testing intermediate outputs.

For the CIFAR10 dataset, we visualize planned two-dimensional tours inspired by the class specific vectors. One option is to consider a grand tour-like approach, where we generate a collection of twodimensional frames by picking them uniformly at random from the set of such frames embedded in the space spanned by the ten class specific vectors. A second option is to restrict our attention to two-dimensional frames that are generated from pairs of the class-specific vectors by using frames of the form  $[\theta_j, \theta'_k]$  where  $\theta'_k$  is the component of  $\theta_k$  that is orthogonal to  $\theta_j$  in order to explore the centered data  $X - \bar{x}$ . Note that we can equivalently use frames of the form  $[r_j, r'_k]$  where  $r'_k$  is the component of  $r_k$  orthogonal to  $r_j$  to explore  $(X - \mathbf{1}\bar{x}^{\mathsf{T}})Q_{\theta}$  for better computational efficiency. For example, we consider a mechanical tour, where we use the frames generated by the pairs plane versus truck, car versus truck, car versus ship, and plane versus ship.

In general, we see that the planned tour strategy works much better compared to the grand tourlike strategy in the sense that the planned tours creates animations that are more interpretable and show more interesting features. For example, for layer 56 in the grand tour-like approach, we can see some key features of the network. We see that the ten groups form comet like formations that point away from a shared common core. However beyond this, it is difficult to tell any relational information between the clusters. In contrast, for layer 56 in the mechanical tour approach, we see that the comets are much more clearly defined and we can extract additional information from the plots. For example, we notice that for each frame, all classes have comets that generally point upwards and to the right.



#### Example Tour of the Swiss Roll Manifold

Figure 12: The plots show a possible path that could be seen on a tour on the Swiss Roll Manifold [15]. We start from a top-down perspective at t = 0 to a side-on perspective by t = 1. At each  $t \in [0, 1]$  we move between these two perspectives with constant speed.

We also note that there is quite a bit of curvature within particular pairs, like how the truck points appear to bend into the cars three seconds in. We also note that at this point, the other eight groups overlap quite a bit. In contrast, for the frame of trucks vs planes at the very start, we notice that the trucks and planes points form orthogonal comets, and the rest of the eight groups spread out much more from one another.

This can also be seen in layer 30 within the VGG15 model, where the grand tour-like approach has comet like formations moving away from a common core, but the planned tour showcases how these spokes are typically orthogonal. For the car versus truck frame, we note that all of the eight other groups mainly cluster around the origin, meaning that they have negligible components in the class specific axes associated with cars and trucks. In comparison, for the plane versus ship axis, we see that most of the groups tend to stick to the origin. The lone exception is cars, which has a distinctly negative ship component. These are distinct features that are much harder to visualize within the grand tour-like approach.

We perform a similar visualization for FashionMNIST intermediate outputs within the ResNet50 model. Again we consider a grand tour-like approach, selecting randomly generated frames from the span of the ten principal axes. We also consider two planned tours where we look at frames generated by pairs of class specific vectors. The first tour is composed of pairs of classes that are rarely confused for one another: t-shirt/tops versus ankle boots, trousers versus ankle boots, trousers versus bags, and t-shirt/tops vs bags. The second tour is composed of classes that are associated with upper-body clothing: t-shirt/tops versus shirts, pullovers versus shirts, pullovers versus coats, and t-shirt/tops versus coats.

When we visualize these tours, we see that the same trends as the CIFAR10 data persist. For example, in layer 141 of the grand tour-like approach, we again notice that the different groups form comet like shapes. However, beyond this, it's hard to observe any trends about how the comets are

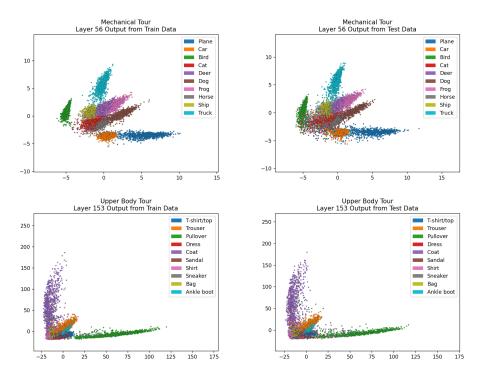


Figure 13: The plots show frames shown within the mechanical tour of the intermediate outputs of the VGG15 model (top row) and the ResNet50 model (bottom row). We can see several differences both between the two models as well as with the intermediate outputs of the training (left column) and testing data (right column).

oriented about one another in space. When we move towards the rarely confused and upper-body planned tours, we can see other interesting features within the data. For layer 141 of the upper-body tour, we observe that bags and sandals have no component along the class specific vectors associated with t-shirt/tops, pullovers, shirts, or coats. However, we see that trousers, ankle boots, and sneakers all have fairly positive components along these vectors. Visualizing the rarely confused planed tour of layer 141, we notice that for the frame generated by the ankle boot and trouser class specific vectors, coats have a very large component in both of these vectors, while most other groups have components much closer to zero. We also notice that when we shift to the frame generated by bags and trousers that unlike other groups, bags will form two comet like clusters pointed in opposite directions. These features seen in the planned tours are generally harder to discover within the grand tour-like approach.

There are major differences between the VGG15 and ResNet50 models. One major difference is in how the intermediate points for the testing data compare to the training data. In the VGG15 model, we notice that in later layers that the class specific clusters from training data will form comets pointing away from a shared core, but their tails will overlap with one another. In contrast, the training data will have a similar shape and position, but their tails will not reach as far down and thus do not overlap. This can be seen prominently in layer 50 of the mechanical tour amongst the testing data and training data. This same effect can be seen to a much more limited extent in the ResNet50 model for layer 153 for the training data and the testing data for the pullovers class, but the effect is not as common among the other groups and layers. This is likely an indicator that the VGG15 model is more overtrained compared to the ResNet50 model.

A second difference is in the shape of the arms. We notice that in general, the comet-shapes for the class specific clusters for the ResNet50 model are fairly sharp and extend out fairly far. Specifically, we see fairly sharp arms for the rarely confused tour on the intermediate training output for layer

151 and for layer 163. We note that the arms frequently extend out as more than 100 away from the origin, and become extremely sharp, especially on layer 163. In contrast, with layer 42 and layer 56 of the mechanical tour on the intermediate training data, we notice that the arms only extend out to at most 40, and the arms are much thicker. This is especially pronounced in layer 56 where the comets are much shorter and wider.

The final difference is in how fast the arms form. We notice that in the ResNet50 model, the arms have formed as early as layer 49 for the training data in the rarely confused tour, which is only about a fourth of the way through the model. Although some classes haven't well differentiated well from others, some groups like bags and trousers have already spread away and formed arms away from the center. In contrast, the arms develop much later in the VGG15 model. We only see the arms clearly develop by about layer 30 for the training data in the mechanical tour, which is about halfway through the model.

### 6 In-group Clustering

In our t-SNE plots we saw strong evidence of two kind of bag images. That evidence was present in intermediate layers but had disappeared by the final layers. In this section we use class-specific projections to make a systematic search for such subclusters and also identify examples of extreme images so a human can interpret them.

At each intermediate layer we project the observations from class k on the vector  $\theta_k$  to rank images from most typical of their class to least typical. We normalize  $N_k$  values to have mean zero variance one when taken over all ten classes, not just class k. so that they have mean square one.

Figure 14 shows those histograms for the images of bags. A bimodal pattern becomes clear by layer 27 if not earlier, and then becomes quite pronounced. By final layer the modes are not very separated, nearly touching. Recall that in the t-SNE plot those points had merged into a single cluster. The top panel in Figure 17 shows images of the bags at the extreme ends of the histogram for the final layer. These represent two quite different kinds of image. Although the final histogram is less bimodal than the earlier ones we still see two very different image types. It is intuitively reasonable that these bag images look different in early network layers that are forming image features. It is also plausible that a network trained to distinguish bags from other image types without regard to what type of bag they are would in its later layers treat them similarly. It would take further research to understand why the gap closes so late in the pipeline instead of earlier.

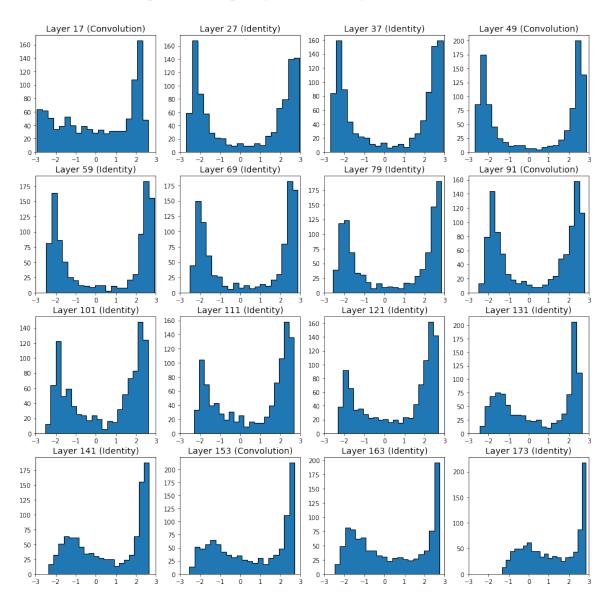
The class-specific projection gives us a tool to look for subclasses. Figure 16 shows histograms for trouser images. There we see no bimodal structure and Figure 17 shows no especially striking difference between the most and least typical trouser images.

Figure 15 shows layer by layer histograms for images of sandals. The sandal images are bimodal at intermediate layers despite the t-SNE images not placing the images into two clear groups. As with bags, these histograms become much less bimodal at later layers. The bimodality disappears much earlier for sandals than for bags. The histograms for sandals become more skewed. From Figure 17 we see a sharp distinction between the types of sandals. The histogram is distinguishing flat ones from high healed ones.

In this section we have looked for two kinds of image by checking the extreme entries in a linear ordering. We expect that more elaborate clustering methods could work when an image class has three or more types. Our main point is that looking at intermediate layers gives additional insights.

### 7 Conclusions

We have presented some graphical methods for probing neural networks layer by layer. In doing so we saw that some clustering within a class can become muted or even disappear as data progress through layers.



#### Histogram of Bag Ouputs on Group Axis, Normalized

Figure 14: Histograms of the intermediate outputs for test images labeled as bags for the outputs of the 16 residual units in the FashionMNIST network.

We devised class-specific projections and found that they can help identify differences among image types within a class. We had to make several choices in defining class-specific projections. We believe that our choices are reasonable but we also believe that other choices could reveal interesting phenomena.

The class-specific projections also provide very focussed looks at point clouds when incorporated into dynamic projections (tours). We saw a big difference between the organization of early layer outputs when comparing a network that was trained using transfer learning from ImageNet and one that was trained from a random start. We saw a variant of neural collapse wherein the outputs form ellipsoidal clusters instead of spherical ones.

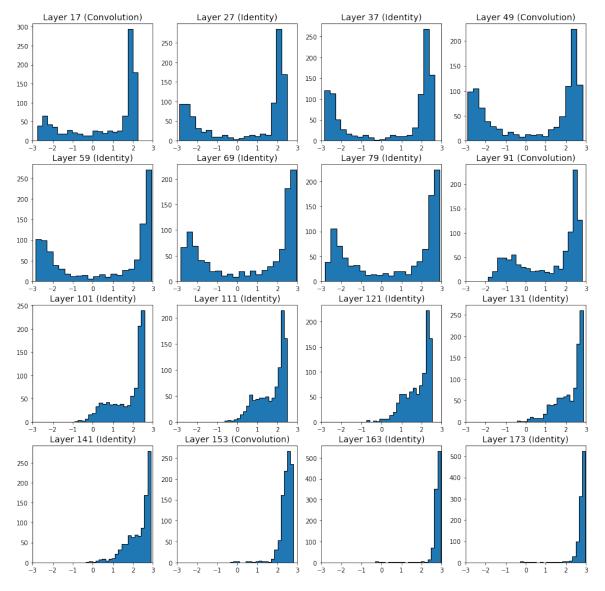
### Acknowledgments

This work was supported by a grant from Hitachi Limited and by the US National Science Foundation under grant IIS-1837931. We thank Masayoshi Mase of Hitachi for comments and discussions about explainable AI.

### References

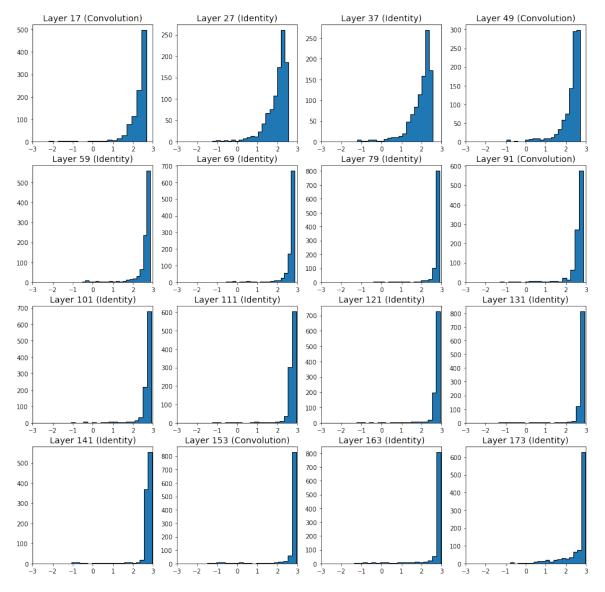
- G. Alain and Y. Bengio. Understanding intermediate layers using linear classifier probes. Technical report, arXiv:1610.01644, 2016.
- [2] D. Asimov. The grand tour: a tool for viewing multidimensional data. SIAM journal on scientific and statistical computing, 6(1):128–143, 1985.
- [3] A. Buja, D. Cook, D. Asimov, and C. Hurley. Computational methods for high-dimensional rotations in data visualization. *Handbook of statistics*, 24:391–413, 2005.
- [4] L. Chen and A. Buja. Local multidimensional scaling for nonlinear dimension reduction, graph drawing, and proximity analysis. *Journal of the American Statistical Association*, 104(485):209– 219, 2009.
- [5] M. A. A. Cox and T. F. Cox. Multidimensional scaling. In *Handbook of data visualization*, pages 315–347. Springer, 2008.
- [6] Jia Deng, Wei Dong, Richard Socher, Li-Jia Li, Kai Li, and Li Fei-Fei. Imagenet: A large-scale hierarchical image database. In 2009 IEEE conference on computer vision and pattern recognition, pages 248–255. Ieee, 2009.
- [7] L. Derksen. Visualising high-dimensional datasets using PCA and t-SNE in Python. https://towardsdatascience.com/ visualising-high-dimensional-datasets-using-pca-and-t-sne-in-python-8ef87e7915b, 2016. Updated April 29, 2019.
- [8] Kaiming He, Xiangyu Zhang, Shaoqing Ren, and Jian Sun. Deep residual learning for image recognition. CoRR, abs/1512.03385, 2015.
- [9] Alex Krizhevsky. Learning multiple layers of features from tiny images, 4 2009.
- [10] J. B. Kruskal. Multidimensional scaling. Number 11. Sage, 1978.
- W. J. Krzanowski. Between-groups comparison of principal components. Journal of the American Statistical Association, 74(367):703-707, 1979.
- [12] M. Li, Z. Zhao, and C. Scheidegger. Visualizing neural networks with the grand tour. Distill, 5(3):e25, 2020.
- [13] T. Nguyen, M. Raghu, and S. Kornblith. Do wide and deep networks learn the same things? uncovering how neural network representations vary with width and depth. Technical report, arXiv2010.15327, 2020.
- [14] V. Papyan, X. Y. Han, and D. L. Donoho. Prevalence of neural collapse during the terminal phase of deep learning training. *Proceedings of the National Academy of Sciences*, 117(40):24652–24663, 2020.
- [15] J. Tenenbaum, V. Silva, and J. Langford. A global geometric framework for nonlinear dimensionality reduction. *Science*, 290(5500):2319–2323, 2000.

- [16] W. S. Torgerson. Multidimensional scaling: I. Theory and method. Psychometrika, 17(4):401– 419, 1952.
- [17] Laurens Van der Maaten and Geoffrey Hinton. Visualizing data using t-SNE. Journal of machine learning research, 9(11), 2008.



## Histogram of Sandal Ouputs on Group Axis, Normalized

Figure 15: Histograms of the intermediate outputs for test images labeled as sandals for the outputs of the 16 residual units in the FashionMNIST network.



### Histogram of Trouser Ouputs on Group Axis, Normalized

Figure 16: Histograms of the intermediate outputs for test images labeled as trousers for the outputs of the 16 residual units in the FashionMNIST network.

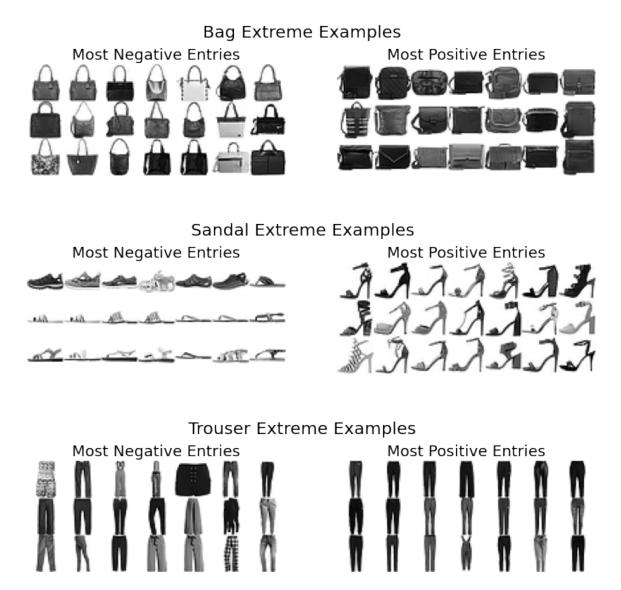


Figure 17: The most extreme examples of three groups along their group specific axis as intermediate outputs of the last residual unit (layer 173) for FashionMNIST.